TUDelft

Delft University of Technology

Document Version
Final published version

Citation (APA)
Novikov, A., & Voskov, D. V. (2025). Interpolation Strategies for Complex Thermal-Multiphase-Reactive Modeling With Operator-Based Linearization. In *Society of Petroleum Engineers - SPE Reservoir Simulation Conference, RSC 2025* Article SPE-223919-MS (SPE Reservoir Simulation Symposium Proceedings; Vol. 2025-March). Society of Petroleum Engineers (SPE). https://doi.org/10.2118/223919-MS

SPE-223919-MS

Interpolation Strategies for Complex Thermal-Multiphase-Reactive Modeling With Operator-Based Linearization

A. Novikov, TU Delft; D. V. Voskov, TU Delft, Stanford University

Abstract

The effective management of geo-energy systems heavily relies on robust modeling frameworks that integrate diverse simulation capabilities, including flow and transport, phase equilibrium, geochemistry and geomechanics. While a multiphysics simulation engine within a unified framework has its advantages, integrating specialized modeling packages often enhances viability. Efficient and seamless communication between these engines be- comes crucial for improving the performance and scalability of the integration. Advanced parametrization tech- niques can facilitate this integration by efficiently approximating and interpolating coupling data, ensuring both speed and accuracy. In this study, we compare the efficiency of different interpolation techniques used for the parametrization of complex many-component fluid systems in compositional simulation. We employ an Operator- Based Linearization (OBL) framework that leverages the general formulation of corresponding conservation laws. OBL effectively learns the operators required for assembly of the laws while interpolation delivers fast evalua- tion of operators and their derivatives for all physical states in a simulation domain. Multilinear interpolation is a simple and robust approach, yet it has poor scaling properties with respect to the dimension of the physical state. To alleviate interpolation costs in multiple dimensions, we study the performance and accuracy of other interpolation techniques, including linear interpolation with standard and Delaunay triangulation. Overall, this approach provides great flexibility, saves development costs and simplifies the incorporation of thermodynamics and geochemistry engines for precise modeling of phase equilibrium, reactive transport, dissolution-precipitation and kinetics of chemical reactions. This research extends the scalability of the OBL framework and addresses the challenges of high dimensionality in compositional modeling. Consequently, this approach holds significant potential for integrating various complex multiphysics problems, enabling the creation of more comprehensive digital twins for geo-energy systems management.

Introduction

Recent projections indicate a substantial rise in electricity demand, estimated at approximately 20% over the next decade (McGeady, 2024). A sustainable approach to meeting this growing demand is barely possible without the efficient development and management of geo-energy resources, including geothermal energy, CO_2 and hydrogen storage sites. Effective management of these sites heavily relies on robust modeling

frameworks that integrate diverse simulation capabilities, including flow and transport, phase equilibrium, geochemistry and geomechanics. While a multiphysics simulation engine within a unified framework has its advantages, integrating specialized modeling packages often enhances viability. Efficient and seamless communication between these engines, therefore, becomes crucial for improving the performance and scalability of the integration.

The choice of primary unknowns is a critical factor that affects the efficiency and flexibility of the reservoir simulation framework. Natural formulation considers pressures, saturations and phase mole fractions as primary unknowns (Coats, 1980). This formulation incorporates not only conservation equations but also equilibrium rela- tions and normalization constraints. While the Jacobian assembly is relatively straightforward, phase appearance and disappearance necessitate variable switching, complicating simulations, especially under parallel computing architectures. Alternatively, molar formulation treats component compositions as primary unknowns (Acs et al., 1985; Collins et al., 1992). It maintains the same number of unknowns across all states, avoiding the necessity of Jacobian reduction and variable substitution. Rigorous comparison of the two formulations is complicated, the related discussion is presented in Voskov and Tchelepi (2012); Zaydullin et al. (2013); Young (2022).

The extension of multiphase compositional simulation to reactive flow and fluid-solid chemical interactions further influences the choice of primary unknowns. Element-based approaches, which formulate balance equa- tions with respect to chemical elements rather than components, can significantly reduce the number of primary unknowns in systems with numerous chemical reactions (Fan et al., 2012). These approaches eliminate equi- librium reaction rate terms while addressing kinetic and equilibrium reactions (Kala and Voskov, 2020). The comparison of natural and molar formulations in reactive flow modeling has been performed in Farshidi et al. (2013). For systems involving dissolution-precipitation reactions, additional unknowns, such as volume fractions of rock matrix constituents, are introduced. This kind of reaction further amplifies the nonlinearity of the overall system introducing porosity-permeability alterations.

In reservoir simulation, the Operator-based Linearization (OBL) simplifies and accelerates Jacobian assem- bly of coupled reactive flow, transport and phase equilibrium modeling (Voskov, 2017). Instead of focusing on subproblems, OBL considers the operator-form of balance equations with localized state-dependent operators, i.e. functions of single-cell unknowns. State-dependent operators are sampled at a limited number of supporting points in the state space, while fast interpolation strategies provide evaluation between supporting points. Consequently, the Jacobian and residual assembly benefits from the evaluation of operators at supporting points shared among all cells, iterations, timesteps and even model runs. OBL has been successfully extended to support buoyancy and capillarity effects (Lyu et al., 2021) and applied in modeling of geothermal sites (Khait and Voskov, 2018), CO_2 storage (Lyu and Voskov, 2023), in the presence of chemical reactions (Kala and Voskov, 2020; de Hoop et al., 2024; Ahusborde et al., 2024), with further optimization on GPU platforms (Khait and Voskov, 2021).

However, the performance and accuracy of OBL depend heavily on its interpolation strategies. While OBL employs linear and multilinear interpolations for fast and convexity-preserving interpolation, these methods re- quire numerous supporting points to resolve nonlinear operators. Insufficient resolution can impair nonlinear convergence, resulting in successive timestep cuts. Multilinear interpolation may provide higher accuracy but suf- fers from exponential complexity as state space dimensionality increases. Conversely, linear interpolation scales linearly with dimensionality which makes it more suitable for many-component mixtures.

In this paper, we evaluate different interpolation strategies in terms of robustness, accuracy, performance and scalability. As test models, we consider compositional multicomponent fluid models with thermal and reactive effects relevant to CO2 sequestration applications. While multilinear interpolation demonstrates its robustness in lower-dimensional spaces, linear interpolation gains superiority in higher dimensions due

to better performance scaling. We investigate the robustness and efficiency of Delaunay and standard triangulation for compositional systems with a large number of components.

Governing Equations

The modeling of mass and energy transport in the subsurface relies on the corresponding conservation laws. The balance of property A can be represented in the following integral form

$$\int_V \frac{\partial a_A}{\partial t} dV + \int_{\partial V} \mathbf{q}_A \cdot \mathbf{n} dS - \int_V r_A dV = 0, \tag{1}$$

where a_A, $\mathbf{q}_A$ and r_A are the accumulation, flux and source terms of property A, respectively, $\mathbf{n}$ is an outward unit normal vector to ∂V. The first term in Eq. (1) accounts for the change of property A in the bulk of volume V caused by the change of thermodynamic state, i.e. change in pressure, fraction or temperature. The second term in Eq. (1) considers fluxes of property A over the boundary ∂V of volume V. The last term in Eq. (1) represents sources (or sinks) of property A situated inside volume V.

For the mass balance of component i in the multiphase multicomponent fluid flow in porous media, we have

$$a_i = \varphi \sum_\alpha^{np} x_{i\alpha} S_\alpha \rho_\alpha, \quad \mathbf{q}_i = \sum_\alpha^{np} \mathbf{q}_{i\alpha} = \sum_\alpha^{np} \left(x_{i\alpha} \rho_\alpha \mathbf{W}_\alpha + \mathbf{j}_{i\alpha} + \mathbf{d}_{i\alpha} \right), \quad r_i = \sum_\alpha^{np} x_{i\alpha} \rho_\alpha r_\alpha, \tag{2}$$

$$\mathbf{w}_\alpha = -\frac{\mathbf{K} k_{r\alpha}}{\mu_\alpha} \left(\nabla p_\alpha - \rho_\alpha M_\alpha g \nabla z \right), \quad \mathbf{j}_{i\alpha} = -\varphi s_\alpha D_{i\alpha} \nabla \left(\rho_\alpha x_{i\alpha} \right), \quad \mathbf{d}_{i\alpha} = -E_{i\alpha} |\mathbf{w}_\alpha| \nabla \left(\rho_\alpha x_{i\alpha} \right), \tag{3}$$

where the subscripts $i = 1, ..., n_c$ and $\alpha = 1, ..., n_p$ denote fluid components and fluid phases, respectively, φ is porosity, $x_{i\alpha}$ is molar fraction of component i in phase α, ρ_α is phase molar density, s_α is volume fraction (saturation) of phase α, $\mathbf{q}_{i\alpha}$ is total velocity of mass of component i in phase α, r_α is molar phase rate. Phase Darcy $\mathbf{w}_\alpha$, molecular diffusion $\mathbf{j}_{i\alpha}$ and dispersion $\mathbf{d}_{i\alpha}$ velocities are defined in Eq. (3), where $\mathbf{K}$ is permeability tensor, $k_{r\alpha}$ is relative phase permeability, μ_α is phase viscosity, p_α is phase pressure, M_α is phase molar weight, g is gravitational acceleration, z is depth, $D_{i\alpha}$ is scalar molecular diffusion coefficient, $E_{i\alpha}$ is scalar dispersivity coefficient. Here we limit our consideration of both molecular diffusion and dispersion fluxes to corresponding Fickian terms.

For the energy balance of multiphase multicomponent fluid flow in porous media, we have

$$\mathbf{i} \, a_e = (1 - \varphi) \rho_s U_s + \varphi \sum_\alpha^{np} s_\alpha \rho_\alpha \left(U_\alpha - gz \right), \text{L} \tag{4}$$

$$\mathbf{q}_e = (1 - \varphi) \kappa_s + \sum_\alpha^{np} \left(h_\alpha - gz \right) \left(\rho^\alpha \mathbf{W}_\alpha + \sum_l^{nc} \left(\mathbf{j}_{i\alpha} + \mathbf{d}_{i\alpha} \right)^- + \varphi_{S_\alpha} \kappa_\alpha, \quad r_e = \sum_\alpha^{np} \rho_\alpha h_\alpha r_\alpha \tag{5}$$

$$\kappa_\alpha = -\lambda_\alpha \nabla T, \quad \kappa_s = -\lambda_s \nabla T, \tag{6}$$

where U_α and U_s are specific (molar) internal energy of fluid phases and rock matrix, h_α is phase enthalpy, κ_α and κ_s are heat conduction velocities of fluid phases and rock matrix, λ_α and λ_s are heat conduction coefficients of fluid phases and rock matrix, T is temperature. Note that while Eq. (6) defines Fourier law of heat conduction, the advection heat fluxes in Eq. (5) account for not only Darcy but also Fickian mass fluxes (R. Byron Bird, 2002). These advection heat fluxes associated with molecular diffusion and dispersion fluxes can be important for model initialization and at the timescale of CO_2 storage applications.

Along with all properties, initial and boundary conditions have to be defined to close the system of Eqs. (2)–(6), the molar fractions of n_c components have to be distributed between n_p phases. We employ

multiphase flash (Michelsen, 1982) to evaluate instantaneous thermodynamic equilibrium between fluid phases. It can be formulated as a set of equations (Wapperom et al., 2023)

$$x\alpha, x_{i\alpha} = \underset{X\alpha, X_{i\alpha}}{\text{aremin}} \; G, \quad G = \frac{G}{RT} = \sum_{\alpha}^{n_p} x_{\alpha} \sum_{i}^{n_c} x_{i\alpha} \ln f_{i\alpha}, \tag{7}$$

$$z_i^0 = \sum_{\alpha}^{n_p} X_{\alpha} X_{i\alpha} \tag{8}$$

$$\sum_{\alpha}^{n_p} x_{\alpha} = \sum_{i}^{n_c} x_{i\alpha} = 1, \quad 0 \le x_{\alpha} \le 1, \quad 0 \le x_{i\alpha} \le 1, \quad \alpha = 1 \dots n_p, \quad i = 1 \dots n_c, \tag{9}$$

where G is the specific (molar) Gibbs energy of fluid mixture, R is gas constant, x_{α} is molar fraction of phase α, $f_{i\alpha}$ is fugacity of component i in phase α, z_i^0 is initial fluid composition (i.e. overall molar fraction of component i) which must be preserved here. Eq. (7) defines the nonlinear optimization problem subjected to mass conservation Eq. (8) and normalization Eq. (9) constraints. Frequently, this problem is reformulated in terms of necessary extremum conditions postulating equal component fugacities $f_{i\alpha} = f_{i\beta}$ among all α, β = 1 … n_p phases.

OBL approach

Efficient solution of the coupled system of Eqs. (1)–(9) is challenging. Although the spatiotemporal discretiza- tion of balance equations is well-established (K. Aziz, 1979), integrating these equations with the phase equilib- rium problem often requires significant development and computational costs. In addition to the complexity of differentiating cumbersome operator expressions, the primary difficulty lies in finding thermodynamic equilib- rium defined in Eqs. (7)–(9), which can be challenging even for two-phase fluid. Many simulation frameworks employ automatic differentiation technique to reduce development cost (Younis and Aziz, 2007; Zhou et al., 2011; Moyner, 2024), which is prone to compromising computational efficiency. Operator-based linearization (OBL) is designed to overcome these challenges by simplifying the treatment of state-dependent operators, providing efficient and flexible means for Jacobian and residual assembly (Voskov, 2017; Lyu et al., 2021).

The efficiency of OBL stems from the localization of state-dependent operators, i.e. functions of single-cell unknowns $\boldsymbol{\omega} = \{p, z, T\}$, called a state. Once discretized in space and time, the balance equations can be rep- resented through state-dependent operators. OBL unifies the evaluation of these operators and their derivatives across all cells in a computational grid. Instead of calculating them in many states, OBL introduces a multidimensional grid covering state space, sampling operators at a predefined set of states and interpolating values between these states. Moreover, it has been found that, for many problems, the region of interest is localized in state space, forming a narrow path between injector and producer states. Consequently, only a limited number of exact opera- tor evaluations are required, while the use of an efficient interpolation strategy ensures a remarkable reduction in computational cost. This approach enables the Jacobian and residual assembly to leverage cached operator values shared across all cells in a computational grid, nonlinear and time iterations, and even multiple simulation runs.

Space-time discretization

We discretize the coupled system of Eqs. (1)–(6) using the Finite Volume Method (FVM) that employs the first-order backward Euler time integration, first-order single-point upstream weighting (SPU) and the two-point flux approximation (TPFA). Applying FVM to the mass balance of component i in Eq. (1), we have the following discrete analogue written in the operator residual form

$$R_i = V\varphi_0\big(\alpha_i(\omega^{n+1}) - \alpha_i(\omega^n)\big) + \Delta t \sum_{l\in L}\sum_\alpha^{np} \mathbf{q}_{i\alpha,l}^{n+1}\cdot\mathbf{n}_l - \Delta t V r_i\big(\omega_{l\alpha}^{n+1}\big) = 0, \quad i = 1\ldots n_c, \tag{10}$$

where R_i is the residual of mass balance equation of fluid component i, V is cell volume, φ_0 is initial porosity, $\omega = \{p, z_i, T\}$ is vector of unknowns (state), superscripts n and $n + 1$ denote the property taken at current and next time steps respectively, Δt is time step, the sum over $l = \{1, 2\} \in L$ represents the summation over cell 1 connections with cell 2, and the following mass operator definitions are used

$$\alpha_i(\omega) = \big(1 + c_s(p - p_{ref})\big)\sum_\alpha^{np} x_{i\alpha}S_\alpha\rho_\alpha, \quad \mathbf{q}_{i\alpha,l}^{n+1}\cdot\mathbf{n}_l = \beta_{i\alpha}\big(\omega_{l\alpha}^{n+1}\big)w_{\alpha,l}^{n+1} + j_{i\alpha,l}^{n+1} + d_{i\alpha,l}^{n+1}, \tag{11}$$

$$\beta_{i\alpha}(\omega) = x_{i\alpha}\rho_\alpha k_{r\alpha}/\mu_\alpha, \quad \gamma_{i\alpha}(\omega) = \big(1 + c_s(p - p_{ref})\big)S_\alpha D_{i\alpha}, \quad \delta_{i\alpha}(\omega) = \rho_\alpha x_{i\alpha}, \tag{12}$$

$$w_{\alpha,l} = \Gamma\big[\big(p_1 - p_{\alpha,cap}(\omega_1)\big) - \big(p_2 - p_{\alpha,cap}(\omega_2)\big)\big] - \big(\rho_\alpha(\omega_1) + \rho_\alpha(\omega_2)\big)g(z_2 - z_1)/2, \tag{13}$$

$$j_{i\alpha,l} = \big(\varphi_{0,1}\gamma_{i\alpha}(\omega_1) + \varphi_{0,2}\gamma_{i\alpha}(\omega_2)\big)\Gamma_d\big[\delta_{i\alpha}(\omega_1) - \delta_{i\alpha}(\omega_2)\big]/2, \tag{14}$$

$$d_{i\alpha,l} = \big(E_{i\alpha,1} + E_{i\alpha,2}\big)\big(|w_{\alpha,1} + w_{\alpha,2}|/2\big)\Gamma_d\big[\delta_{i\alpha}(\omega_1) - \delta_{i\alpha}(\omega_2)\big]/2, \tag{15}$$

where c_s is rock compressibility, p is pressure of reference fluid phase which depends on specific form of $p_{\alpha,cap}(\omega)$, p_{ref} is reference pressure defining initial porosity $\varphi_0 = \varphi(p_{ref})$, subscript $l\alpha$ denotes the property evaluated using SPU approximation:

$$\omega^{l\alpha} = \begin{cases} \omega_1, & w_{\alpha,l} > 0, \\ \omega_2, & w_{\alpha,l} \le 0, \end{cases} \tag{16}$$

Γ is Darcy flux transmissibility evaluated for heterogeneous permeability field, Γ_d is geometrical part of trans- missibility, i.e. evaluated for a homogeneous field, $p_{\alpha,cap}$ is phase capillary pressure. The approximations in Eqs. (13)–(15) are the combination of arithmetic averaging and TPFA applied for Darcy w_α, molecular diffusion $j_{i\alpha}$ and dispersion $d_{i\alpha}$ fluxes

$$w_\alpha = -\mathbf{K}\mathbf{n}\cdot\big(\nabla p_\alpha - \rho_\alpha M_\alpha g\nabla z\big), \quad j_{i\alpha} = -\varphi s_\alpha D_{i\alpha}\mathbf{n}\cdot\nabla\delta_{i\alpha}, \quad d_{i\alpha} = -E_{i\alpha}|w_\alpha|\mathbf{n}\cdot\nabla\delta_{i\alpha}, \tag{17}$$

where cell-centered Darcy phase velocities $\mathbf{w}_{\alpha,1}$ and $\mathbf{w}_{\alpha,2}$ are reconstructed from corresponding phase fluxes as

$$\mathbf{w}_\alpha = \big(\mathbf{A}^T\mathbf{A}\big)^{-1}\mathbf{A}^T \begin{matrix} \beta_{i\alpha}\big(\omega_{l\alpha}^{n+1}\big)w_{\alpha,0}^{n+1} \\ \vdots \\ \beta_{i\alpha}\big(\omega_{l\alpha}^{n+1}\big)w_{\alpha,l}^{n+1} \end{matrix}, \quad \mathbf{A} = \begin{matrix} S_1\mathbf{n}_1 \\ \vdots \\ S_1\mathbf{n}_1 \end{matrix}, \quad l \in L, \tag{18}$$

where S_l is area of the interface corresponding to connection l. Note that well connections do not while boundary conditions do participate in velocity reconstruction in Eq. (18).

Applying FVM to the energy balance equation, the discrete version of Eq. (1) written in operator residual form becomes

$$R_e = V\big(1 - \varphi_0\big)\big(\alpha_{es}(\omega^{n+1}) - \alpha_{es}(\omega^n)\big) + V\varphi_0\big(\alpha_{ef}(\omega^{n+1}) - \alpha_{ef}(\omega^n)\big) + \Delta_t\sum_{l\in L}\mathbf{i}\mathbf{q}_{es,l}^{n+1}\cdot\mathbf{n}_l + \sum_\alpha \mathbf{q}_{e\alpha,l}^{n+1}\cdot\mathbf{n}_l^L - \Delta t V r_e\big(\omega^{n+1}\big) = 0, \tag{19}$$

where the energy operators are defined as

$$\alpha_{es}(\omega) = \big(1 + c_s(p - p_{ref})\big)U_s, \quad \alpha_{ef}(\omega) = \big(1 + c_s(p - p_{ref})\big)\sum_\alpha^{np} s_\alpha\rho_\alpha(U_\alpha - gz) \tag{20}$$

$$\chi_{es}(\boldsymbol{\omega}) = 1 + c_s\left(p - p_{ref}\right), \quad \chi_{e\alpha}(\boldsymbol{\omega}) = \left(1 + c_s\left(p - p_{ref}\right)\right)s_\alpha, \tag{21}$$

$$\mathbf{q}_{es,l}^{n+1} \cdot \mathbf{n}_l = \kappa_{s,l} \quad \mathbf{q}_{e\alpha,l}^{n+1} \cdot n_l = \left(h\alpha\left(\omega_{l\alpha}^{n+1}\right) - gz_l\right)\sum_i^{n_c}\left(\mathbf{q}_{i\alpha,l}^{n+1} \cdot \mathbf{n}_l\right) + \kappa_{\alpha,l}, \tag{22}$$

$$\kappa_{s,l} = \left(\left(1 - \varphi_{0,1}\right)\lambda_{s,1}\chi_{es}(\omega_1) + \left(1 - \varphi_{0,2}\right)\lambda_{s,2}\chi_{es}(\omega_2)\right)\varGamma_d\left[\; T_1 - T_2\right]/2, \tag{23}$$

$$K_{a,l} = \left(\varphi_{0,1}\lambda_{a,1}\chi_{ec}(\omega_1) + \varphi_{0,2}\lambda_{a,2}\chi_{el}(\omega_2)\right)\varGamma_d\left[\; T_l\text{-}T_2\right]/2 \tag{24}$$

where Eqs. (23) and (24) are combinations of arithmetic averaging and TPFA applied to respective heat conduc- tion fluxes

$$\kappa_s = -(1-\varphi)\lambda_s\nabla\;\; T, \quad \kappa_\alpha = -\varphi s_\alpha\lambda_\alpha\nabla T. \tag{25}$$

It is worth to mention that TPFA in Eqs. (13)–(15), (23), (24) can be conveniently replaced with a suitable multi- point flux approximations.

Discretization in state space

OBL approach entails the evaluation of state-dependent operators

$$\left\{\alpha_i, \alpha_{ef}, \alpha_{es}, \beta_{i\alpha}, \rho_\alpha, h_\alpha, \gamma_{i\alpha}, \delta_{i\alpha}, p_{\alpha,\,cap}, \chi_{e\alpha}, \chi_{es}\right\}(\boldsymbol{\omega}) = \mathbf{f}(\boldsymbol{\omega}), \tag{26}$$

at predefined grid nodes ω covering the state space. For regular grid we have

$$\varpi = \bar{p} \times \bar{z} 1 \times L \times \bar{z}_{nc}\overline{T}, \tag{27}$$

$$\bar{p} = \left\{p_{,1}\ldots, p_{N_p}\right\}, \quad \tilde{z}_1 = \left\{z_{1,1}, \ldots, z_{1,N_z}\right\}, \ldots, \widetilde{z_n} = \left\{z_{n_c,1}, \ldots, z_{n_c,N_{nn_c}}\right\}, \quad \overline{T} = \left\{T_1, \ldots, \quad T_{N_T}\right\}, \tag{28}$$

where $\overline{p}, \overline{z}_i$ and $\overline{T}$ denote state-space axes coordinates, $\mathbf{f}$ is interpolant function used to reconstruct operator values between supporting points. Regular grid guarantees fast evaluation of derivatives. The distribution of points along axes in Eq. (28) can be dictated by specific model properties, e.g. for better resolution of phase envelope. By default, they are distributed uniformly for simplicity. Once operators have been evaluated at a certain point, they are stored in a multidimensional table and can be used for the evaluation of operators and their derivatives in adjacent hypercubes. The state space dimension is equal to $n_d = n_c$ for isothermal simulation and $n_d = n_c + 1$ for thermal one.

We consider two strategies of operator sampling at supporting points $\boldsymbol{\omega}$: static and adaptive. In *static sampling*, operators are pre-evaluated at all supporting points within the state space before the simulation begins. During the simulation, no new points are evaluated; instead, interpolation is performed over the precomputed operator values. This approach eliminates the computational overhead associated with evaluating new points during sim- ulation, which can be substantial, particularly when coupling with third-party thermodynamics or geochemistry solvers. Static sampling usually brings benefits in simulation scenarios involving multiple model runs with iden- tical fluid properties defined in a relatively low-dimensional state space. However, in higher-dimensional state spaces, precomputing operator values at all grid vertices becomes memory-exhaustive and often redundant.

In contrast, *adaptive sampling* evaluates operators dynamically during simulation. For any requested state, the method identifies the set of supporting points required for interpolation. If any of these points have not yet been evaluated, the exact operator values are computed at those points and stored. As the simulation progresses, the ac- cumulation of operator values reduces the need for additional evaluations, with the majority of exact computations occurring at the beginning of the simulation. Adaptive sampling can achieve significant efficiency gains, particu- larly when requested states are localized within the state space. This makes it well-suited for fluids composed of many components, where parametrization is computationally demanding.

The evaluation of operator values and their derivatives relies on interpolation between exact values at sup- porting points. Various interpolation strategies can be applied, whereas, in this study, we focus on multilinear and linear interpolation strategies. Their key advantages, such as high performance, robustness and convexity- preserving, make them particularly suitable for compositional modeling. The *piecewise multilinear interpolation* is performed over a hypercube by subsequently applying linear interpolation along each axis. The recursive nature of the calculations required for constructing the interpolant results in exponential complexity with respect to state space dimension, i.e. $O(2^n d)$

In *piecewise linear interpolation*, a hypercube is subdivided into simplices, requiring triangulation. We consider standard and Delaunay triangulations. The standard triangulation partitions a hypercube into a set of sim- plices sharing the same vertex. This triangulation simplifies point location and evaluation of barycentric coordi- nates within simplices (Weiser and Zarantonello, 1988). The Delaunay triangulation maximizes minimum angles of the simplices that can reduce interpolation errors. However, the identification of simplex where the input point resides becomes time-consuming. Furthermore, the evaluation of barycentric coordinates for an input point in simplices constructed with Delaunay triangulation requires matrix inversion, which can be pre-calculated for all simplices. Once barycentric coordinates of an input point are known, the evaluation of operators and their derivatives has linear complexity with respect to the state space dimension, i.e. $O(n_d)$.
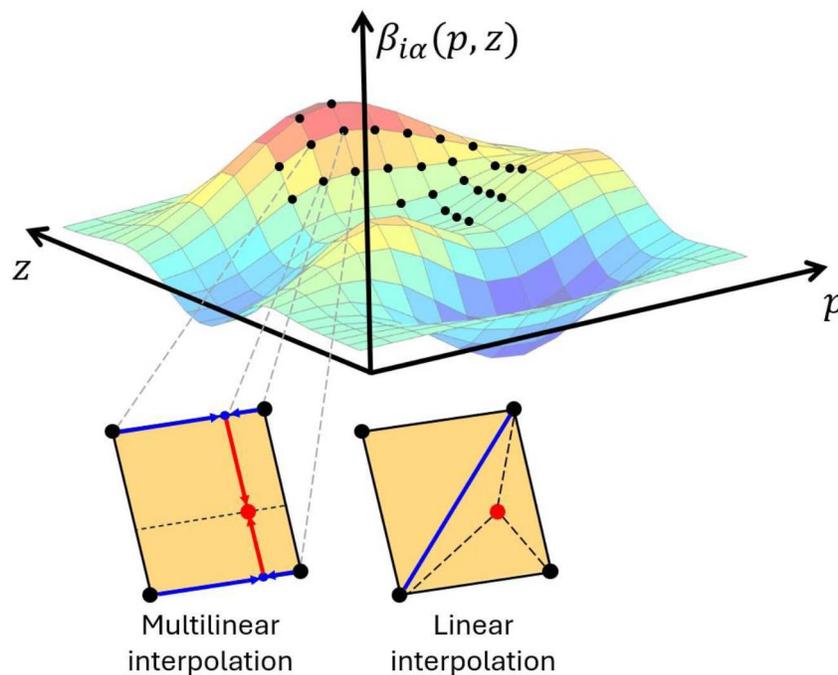
Figure 1—Interpolation of operator $\beta_{i\alpha}$ in pz state space covered by rectilinear grid. Multilinear and linear interpola- tions are considered.

Results

Comparison of interpolation strategies

We analyze and compare various interpolation strategies across three configurations: 1D homogeneous, 2D homogeneous, and 3D heterogeneous reservoirs. For the latter one, we use the dataset from the 10th SPE Com- parative Solution Project (SPE10). The reservoirs in all three setups are fully completed with a pair of injection and production vertical wells. The setups are presented in Fig. 2.

(a) 1D resevoir   (b) 2D reservoir   (c) SPE10
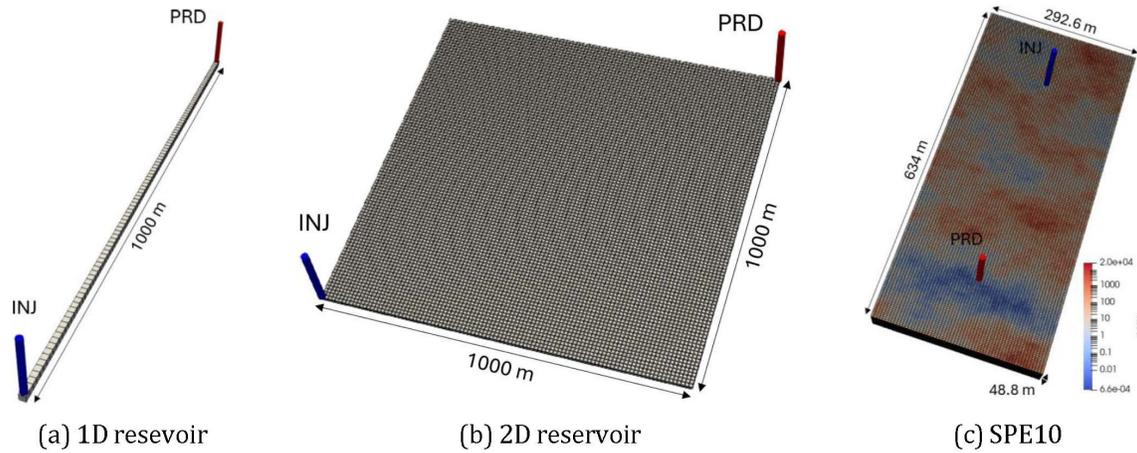
Figure 2—Simulation domain in three configurations: (a) 1D reservoir, (b) 2D reservoir, and (c) SPE10.

Our study focuses on the modeling of the isothermal injection of gaseous CO_2 into the oil-bearing reservoir. The equilibrium of the resulting two-phase multicomponent fluid flow is governed by constant ratios between gas and liquid compositions (K-values) which are listed in Tab. 1. The behavior of interpolation strategies is examined including with respect to varying numbers of fluid components. The particular components and their initial composition corresponding to a certain number of components, n_c, are provided in Tab. 2. For 1D and 2D reservoirs, we initialize the model with a uniform pressure $p_0 = 100$ bar, maintaining a fixed bottom hole pressure at the production well and a constant fluid rate at the injection well until the final time $T = 2$ years. In the SPE10 model, the reservoir is initialized with a gas-oil contact (GOC) and an initial pressure defined at the middle of the reservoir. Below and above the GOC, uniform composition equal to liquid and vapour mole fractions are specified which are calculated from the initial compositions in Tab. 2. In this case, we use the similar well controls running model for $T = 10$ years. All simulations use the adaptive sampling strategy for evaluating supporting points in the state space.

Table 1—Fixed K-values defining equilibrium of a two-phase fluid.

CO_2	C_1	C_2	C_3	C_4	nC_4	C_5	nC_5	C_6	C_7	C_8	C_9
1.5	2.5	2.0	1.0	0.7	0.5	0.4	0.3	0.2	0.15	0.12	0.10

C10	C11	C12	C13	C14	C15	C16	C17	C18	C19	C20	
0.05	0.04	0.035	0.03	0.025	0.02	0.01	0.01	0.01	0.01	0.01	

Table 2—Initial component compositions for different number of components n_c.

n_c	CO_2	C_1	C_2	C_3	C_4	nC_4	C_5	nC_5	C_6	C_7	C_8	C_9	C_{10}	C_{11}	C_{12}	C_{14}	C_{16}	C_{18}	C_{19}	C_{20}
4	.005	.5			.3								.195							
6	.005	.35			.25								.195				.125			.075
8	.005	.35	.17		.15			.125					.1				.075			.025
10	.005	.3	.17		.15		.1	.1	.075				.05				.025			.025
12	.005	.3	.15	.1	.075	.075	.065	.065	.06				.05				.035			.02
20	.005	.24	.12	.09	.07	.07	.06	.06	.05	.045	.04	.035	.03	.025	.02	.015	.01	.007	.005	.003

Figs. 3a and 3b demonstrate composition and gas saturation profiles obtained in 1D and 2D configurations at $t = 1$ yr and $t = 2$ yr, correspondingly. The diagonal cross-section is presented for the 2D reservoir. The results obtained with linear interpolation on standard (LinS) and Delaunay (LinD) triangulations, and multilinear interpolation (MLin) are shown. The results obtained with the coarse resolution of the state

space, $N = 64$ points per each of axes, are compared against the finely resolved one with $N = 1024$ points per axes, treated as a reference solution. The results coincide with each other almost in the whole domain, except for narrow regions around propagating fronts. Comparison of solutions around fronts demonstrates superior accuracy of multilinear interpolation over linear interpolation, regardless of the triangulation method. Moreover, the profiles obtained with Delaunay triangulation exhibit low-frequency oscillations of small amplitude spreading across the whole domain.

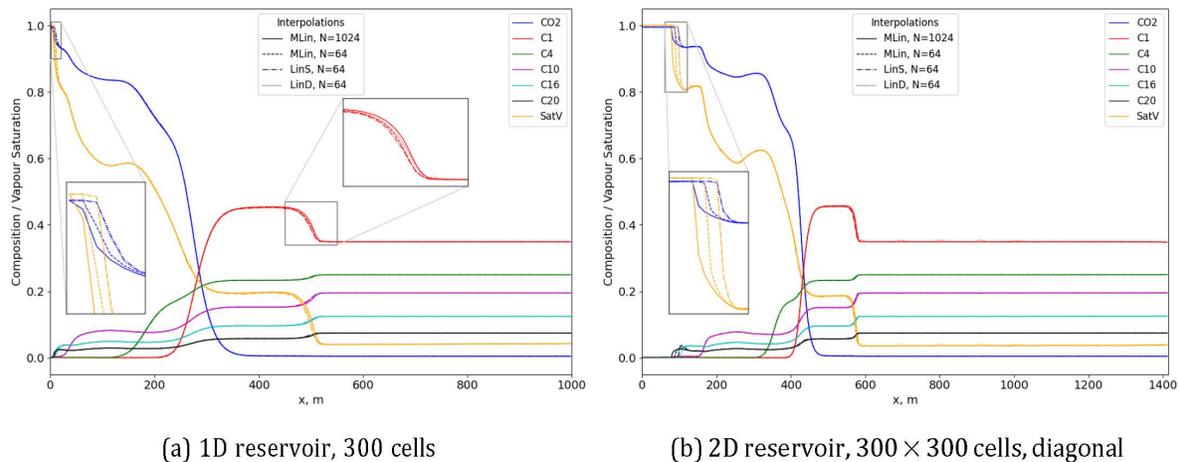(a) 1D reservoir, 300 cells   (b) 2D reservoir, 300×300 cells, diagonal

Figure 3—Composition and gas saturation profiles obtained at $t = 1$ yr for 1D reservoir (a) and at $t = 2$ yr for 2D reservoir (b) using different interpolation strategies, and number of supporting points in the state space of $n_c = 6$ dimension.

Tab. 3 presents performance metrics obtained for linear interpolation on standard (LinS) and Delaunay (LinD) triangulations, and multilinear interpolation (MLin), for $N = 64, 256, 1024$ points uniformly distributed along each axis of the state space. The interpolation and point generation metrics are presented in percentages of total simulation time. We use Newton iterations (NI) to resolve nonlinearities and CPR preconditioner coupled with GMRES iterations (LI) for efficient solutions of linear systems. We can observe the following takeaways from this table:

- Multilinear interpolation delivers significantly better convergence than linear interpolation. Moreover, the coarse linear interpolation can introduce convergence issues, especially with Delaunay triangulation, that waste simulation time.
- In highly resolved state space OBL performance is primarily limited by the point generation for both linear and multilinear interpolations in the first simulation run. Note that in a series of runs sharing the same operators, points are cached and this cost will be significantly reduced. The high relative interpolation time for Delaunay triangulation for 2D setup can be explained by the relatively high cost of simplex identification for given points.
- Delaunay triangulation constructed for linear interpolation not only does not show any benefits over standard triangulation but can significantly worsen nonlinear convergence. The reason for this behavior is a matter of ongoing study.

Table 3—Performance metrics of 1D (left) and 2D (right) setup runs with n_c = 6. Reservoirs are covered by 300 and 300 × 300 cells respectively, keeping the same cell sizes. LinS, LinD denote linear interpolation with Standard and Delaunay triangulations, while MLin stands for multilinear interpolation. N is a number of points uniformly distributed over each axes of the state space. The interpolation and point generation times are given in percent of the total simulation time. TS, NI and LI are the total numbers of time steps, nonlinear and linear iterations respectively. The timesteps and iterations wasted due to lack of convergence are listed in brackets.

		1D setup, 300 cells, n_c = 6							2D setup, 300 × 300 cells, n_c = 6				
Meth.	N	Interp., %	Point gen., %	TS	NI	LI	Meth.	N	Interp., %	Point gen., %	TS	NI	LI
LinS	64	5.7	53.7	203	398	1113	LinS	64	10.2	1.3	207(6)	434(58)	1912(262)
LinS	256	3.3	75.8	203	255	746	LinS	256	11.7	9.7	207(7)	340(70)	1660(345)
LinS	1024	2.7	85.1	203	217	643	LinS	1024	11.4	39.1	206(4)	360(40)	1771(190)
LinD	64	33.3	32.3	203	401	1132	LinD	64	18.0	0.04	613(420)	1201(4193)	4221(15260)
LinD	256	13.6	70.3	203	233	687	LinD	256	34.5	1.6	372(253)	903(2530)	4054(11920)
LinD	1024	8.2	81.1	203	214	634	LinD	1024	49.0	33.7	211(13)	360(130)	1779(601)
MLin	64	3.4	68.8	203	292	838	MLin	64	8.8	7.6	203	319	1521
MLin	256	2.5	92.2	203	220	653	MLin	256	5.7	53.5	203	259	1376
MLin	1024	2.0	95.7	203	213	632	MLin	1024	5.8	80.2	204(1)	250(10)	1348(54)

Tab. 4 presents performance metrics obtained for different numbers of fluid components: n_c = 4, 6, 8, while the state space remains covered by the same uniform grid with N = 128 points per each axis. The results show that

- The multilinear interpolation manages to keep the iteration count low, even with increasing dimensionality. In contrast, the linear interpolation introduces a noticeable increase in iteration count in higher dimensions.
- The multilinear interpolation does not exhibit convergence issues, whereas the linear interpolation produces time step cuts in modeling of 2D setup.
- The multilinear interpolation demonstrates increasing point generation and interpolation costs with the state space dimensionality in the modeling of 2D setup. It is explained by the exponentially increasing number of supporting points ($2^n d$) and by the complexity associated with the interpolation.

Table 4—Performance metrics of 1D (left) and 2D (right) setup runs with $N = 128$. Reservoirs are covered by 300 and 300 × 300 meshes respectively, keeping the same cell sizes. LinS, LinD denote linear interpolation with Standard and Delaunay triangulations, while MLin stands for multilinear interpolation. N is a number of supporting points uniformly distributed over each axes of the state space. The interpolation and point generation times are given in percent of the total simulation time. TS, NI and LI are the total numbers of time steps, nonlinear and linear iterations respectively. The timesteps and iterations wasted due to lack of convergence are listed in brackets.

		1D setup, 300 cells, $N = 128$					2D setup, 300 × 300 cells, $N = 128$					
Meth.	n_c	Interp., %	Point gen., %	TS	NI	LI	Meth.	n_c	Interp., %	Point gen., %	TS	NI	LI
LinS	4	4.4	62.7	203	292	828	LinS	4	10.4	1.5	205(4)	327(40)	1775(206)
LinS	6	5.9	67.2	203	369	1007	LinS	6	11.7	4.4	204(1)	341(10)	1579(50)
LinS	8	7.4	64.3	203	386	1052	LinS	8	12.0	4.6	208(9)	394(90)	1761(414)
LinD	4	32.0	25.4	203	234	667	LinD	4	65.0	1.0	206(6)	328(57)	1786(291)
LinD	6	23.2	56.2	203	298	858	LinD	6	51.9	1.9	228(44)	596(440)	2703(1987)
LinD	8	19.6	44.5	204(1)	378(10)	1050(30)	LinD	8	47.0	2.6	386(315)	1096(3150)	4898(15231)
MLin	4	2.6	53.5	203	220	626	MLin	4	3.2	2.9	203	285	1579
MLin	6	3.3	88.4	203	240	709	MLin	6	7.7	13.3	203	281	1435
MLin	8	3.5	92.3	203	238	697	MLin	8	15.4	30.3	203	277	1425

While the simulation results reported above are limited to rather simplistic homogeneous reservoirs, Tab. 5 presents performance metrics obtained in the modeling of the heterogeneous SPE10 setup. It incorporates simulations performed for various numbers of components with linear (LinS) and multilinear (MLin) interpolation strategies, whereas linear interpolation utilizes standard triangulation. The following findings can be obtained from the table

- The interpolation costs of multilinear interpolation dramatically increases with the dimensionality of the state space, which highlights the exponential complexity of the interpolation.
- Point generation is negligible in a simulation of large-size setups.

Table 5—Performance metrics of SPE10 setup runs. LinS and MLin stand for the linear interpolation on standard triangulation and the multilinear interpolation respectively. N is a number of supporting points uniformly distributed over each axes of the state space of dimension n_c. The interpolation and point generation times are given in percent of the total simulation time. TS, NI and LI are the total numbers of time steps, nonlinear and linear iterations respectively. The timesteps and iterations wasted due to lack of convergence are listed in brackets.

			SPE10 setup, 1122k cells				
Meth.	n_c	N	Interp., %	Point gen., %	TS	NI	LI
LinS	4	128	6.4	0.1	3817	3875	54771
MLin	4	128	1.0	0.07	3817	3845	63305
MLin	6	128	3.4	0.3	3817	3822	43159
LinS	8	128	6.7	0.2	3817	3834	39422
MLin	8	128	11.4	1.5	3817	3820	23458
MLin	10	128	60.6	2.7	3817	3820	9128
LinS	12	128	7.0	0.2	3817(1)	3850(10)	69153(220)

Interpolation in highly-dimensional space

The scalability of interpolation strategies is a critical factor for efficient modeling of many-component fluids. Moreover, improved scalability enables the OBL approach to extend its applicability to a wider range of problems. Previous results (Tab. 5) indicate that multilinear interpolation can demand substantial

simulation resources, even with $n_c = 10$ in large heterogeneous models. In contrast, linear interpolation demonstrates significantly better scalability which makes it a more suitable choice for modeling many-component fluids.

In this section, we present the results of modeling such fluids using linear interpolation with standard trian- gulation (LinS). To explore the limits of the state space dimensionality, we extended the test setup to $n_c = 20$ and performed simulations. The chosen reservoir configuration is a single-layer from the SPE10 setup, produced with an injector-producer well doublet and shown in Fig. 2c. Fig. 4 demonstrates pressure and compositions of 20 components at $t = 91.7$ yr after production. These results show that the injected vapor CO_2 displaces liquid hydrocarbon fractions.
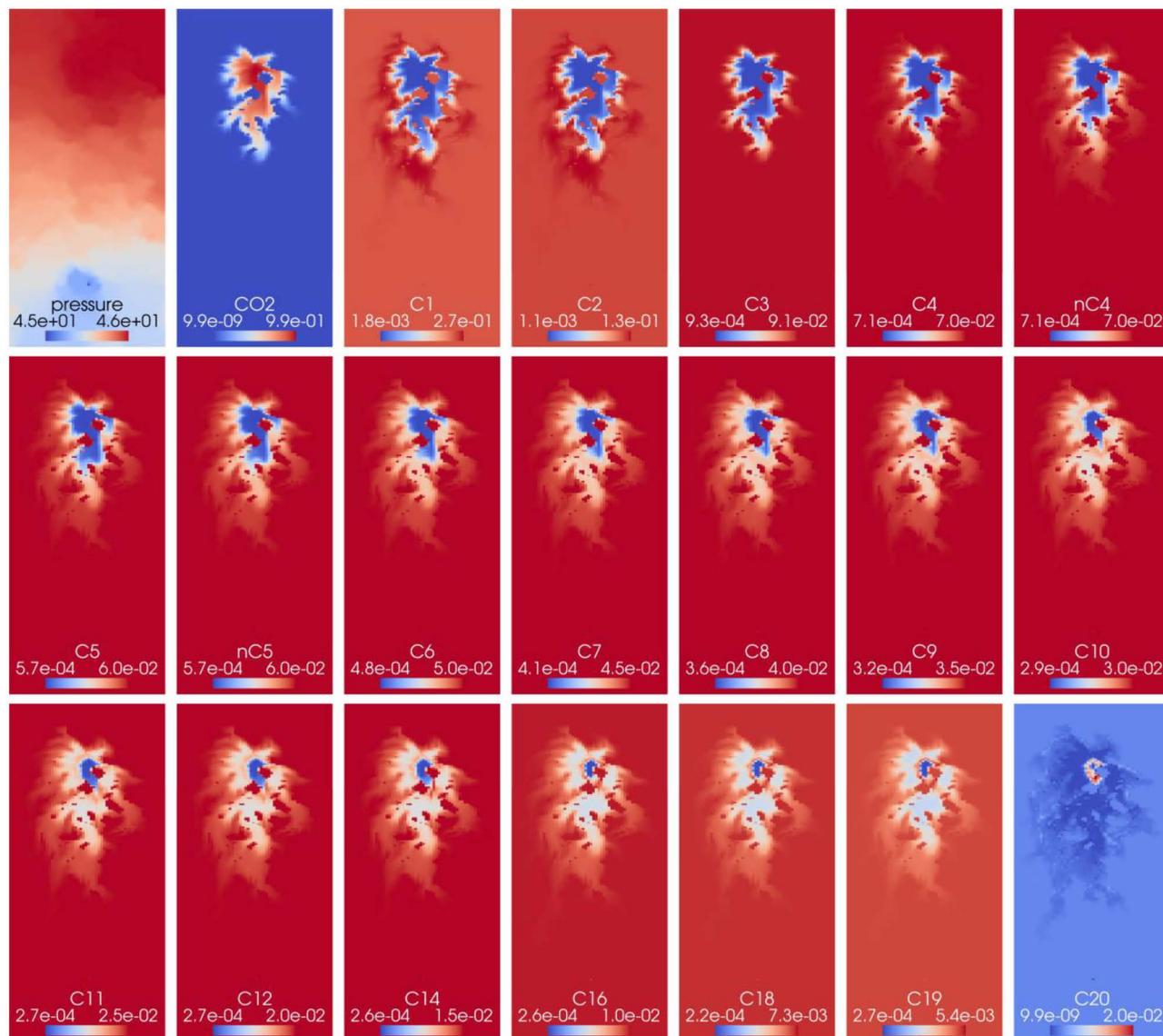

Figure 4—Pressure and compositions for simulation of 20-component fluid in single (top) layer of SPE10 setup.

Tab. 6 presents the performance metrics of simulations conducted with three different resolutions of the state space: $N = 32, 64, 96$. According to the table, the number of linear iterations increases with the resolution of the state space. This trend can be attributed to the better-resolved nonlinear operators, which contrast with smoother approximations obtained at lower resolutions. Consequently, these better-resolved operators require more GMRES iterations to sufficiently suppress residuals.

Table 6—Performance metrics of the modeling of the many-component mixture in a single layer of SPE10 setup. LinS denotes the linear interpolation on standard triangulation, N is a number of supporting points uniformly distributed over each axe of the state space of dimension n_c. The interpolation and point generation times are given in percent of the total simulation time. TS, NI and LI are the total numbers of time steps, nonlinear and linear iterations respectively. The timesteps and iterations wasted due to lack of convergence are listed in brackets.

			single layer of SPE10 setup, 13.2k cells				
Meth.	n_c	N	Interp., %	Point gen., %	TS	NI	LI
LinS	20	32	2.3	0.05	3818(1)	3818(3)	10160(7)
LinS	20	64	1.9	0.09	3817	3817	15340
LinS	20	96	1.6	0.12	3817	3817	19929

## Dissolution-precipitation while CO₂ injection in carbonates

In this section, we demonstrate the results of modeling of dissolution-precipitation of carbonate rock while isothermal CO_2 injection. Fluid flow and reactive compositional transport solver, open-darts (Voskov et al., 2024), are coupled here with a geochemistry solver, PHREEQC (Parkhurst and Appelo, 2013), which resolves both phase equilibrium and reaction kinetics. This combination allows the full complexity of chemical alterations accompanying CO_2 injection to be modeled with relatively low development costs. The performance results demonstrated below underscore the efficiency and flexibility of the OBL approach while coupling multiple solvers.

The modeling of flow and transport in the presence of dissolution-precipitation reactions requires modification of the formulation of balance laws presented above. First, the system of balance Eqs. (1)–(3) must be extended to account for the balance of immobile minerals that constitute rock matrix. We use the volume fraction of these minerals as corresponding primary unknowns. Second, we employ element-based formulation while working with multicomponent reactive flow (Kala and Voskov, 2020). It implies the transformation of component-based bal- ance laws to element-based analogs and changing corresponding primary unknowns from component to element compositions.

At the initial conditions, we consider the following components and the transformation defined by a respective stoichiometric matrix

$$
\begin{array}{c|ccccccccccc}
 & H_2O & H^+ & OH^- & CO_2 & HCO_3^- & CO_3^{2-} & CaCO_3(aq) & Ca^{2+} & CaOH^+ & CaHCO_3^+ & CaCO_3(s) \\
\hline
CaCO_3(s) & 0 & 0 & 0 & 0 & 0 & 0 & 0 & 0 & 0 & 0 & 1 \\
Ca & 0 & 0 & 0 & 0 & 0 & 1 & 1 & 1 & 1 & 1 & 0 \\
C & 0 & 0 & 0 & 1 & 1 & 1 & 1 & 0 & 0 & 1 & 0 \\
O & 1 & 0 & 1 & 2 & 3 & 3 & 3 & 0 & 1 & 3 & 0 \\
H & 2 & 1 & 1 & 0 & 1 & 0 & 0 & 0 & 1 & 1 & 0 \\
\end{array}
\tag{29}
$$

which is filled with stoichiometric coefficients of the elements constituting each of the components. $CaCO_3(s)$ denotes the immobile calcite composing a solid porous matrix, whose volume fraction is treated as a primary un- known. During the simulation, geochemistry solver consider wider range of components appearing and disappear- ing out of given elements. The complete list of species and elements is presented in Fig. 5. The distribution among vapor, aqueous and solid phases are also shown. The species mentioned in Fig. 5a are taken from PHREEQC output and point out that complexation and speciation along with oxidation-reduction, acid-based, methanogene- sis reactions take place. Fig. 5b presents the reduced element system, which alleviates the complexity of solving numerous conservation equations in the flow and transport modeling part.
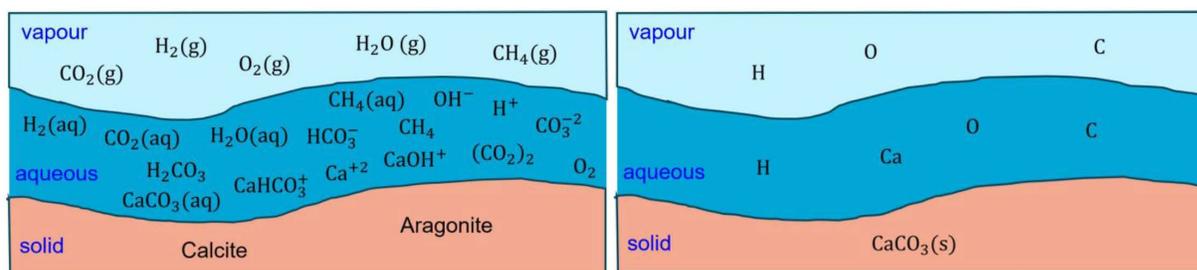
(a) Species participated in geochemistry modeling.   (b) Elements participated in flow and transport modeling.

Figure 5—The species and elements participating in modeling.

We consider two core-scale domain configurations shown in Fig. 6. The first one represents a 1D homoge- neous domain, while the second one is a 2D heterogeneous domain. Both domains are initialized with uniform initial pressure and component compositions which are transferred to element compositions. Besides, both con- figurations are produced with a couple of injection and production wells mimicking the fluid inlets and outlets located at the opposite sides of the domains. The constant pressure p_0 is maintained at the production wells, while a fixed rate of CO_2 water solution is prescribed at the injection well. Both the porosity-permeability relationship and relative phase permeabilities are defined as power laws. The properties used in the simulation are listed in Tab. 7
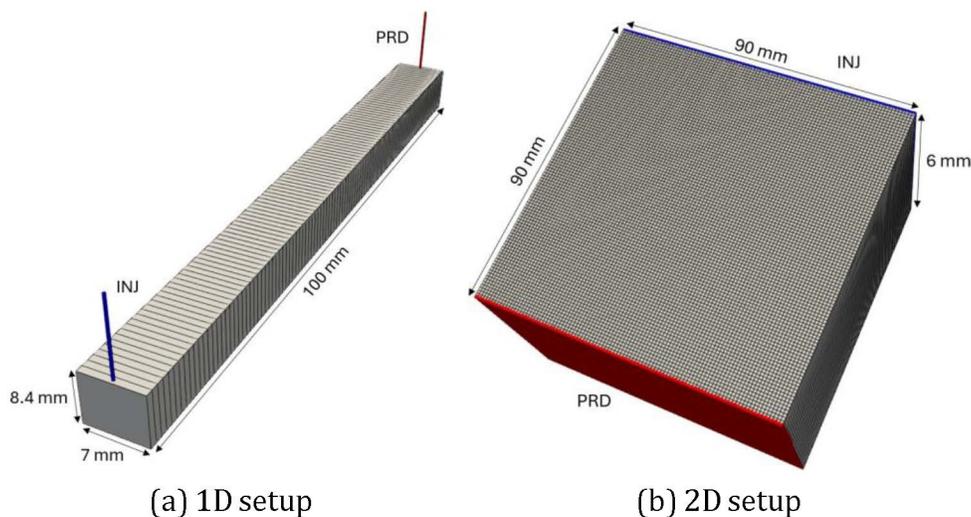

(a) 1D setup   (b) 2D setup

Figure 6—Simulation domain in two configurations: (a) 1D reservoir, (b) 2D reservoir.

Table 7—The properties used in the modeling of calcite dissolution-precipitation.

Property	Value	Unit
Initial pressure, p_0	100	bar
Initial mean porosity, φ_0	0.3	-
Rock density, ρ_s	$\rho_{s0}(1 + c_s(p - p_0))$	kgm^{-3}
Rock initial density, ρ_{s0}	2710	kgm^{-3}
Rock compressibility, c_s	10^{-6}	bar^{-1}
Aqueous phase viscosity, μ_{aq}	CoolProp/IAPWS	cP
Vapour phase viscosity, μ_v	CoolProp/Fenghour et al. (1998)	cP
Porosity-permeability relationship, k	$1.25e+4\times\varphi^4$	mD
Relative phase permeabilities, $k_{r\alpha}$	s_α^2	-
Reaction kinetics		
Acidic reaction order w.r.t. H$^+$, n	1	-
Reactive surface area, Ω	0.925	m^2 mol^{-1}
Temperature, T	323.15	K
Reference temperature, T_{ref}	298.15	K
Reference acidic reaction constant, $k_{ref}^{(a)}$	0.501187234	mol/m^2/sec
Reference neutral reaction constant, $k_{ref}^{(n)}$	1.54882e-6	mol/m^2/sec
Acidic activation energy, $E^{(a)}$	14.4	kJmol^{-1}
Neutral activation energy, $E^{(n)}$	23.5	kJmol^{-1}
Maximum saturation ratio, SR_{max}	100	-
Empiric powers, p, q	1, 1	-
Gas constant, R	8.314472	Jmol^{-1} K^{-1}

The kinetics of chemical reactions is governed by the Arrhenius equation accounting for both acidic (a) and neutral (n) reaction pathways. Thus, the total reaction rate r is represented by the sum of acidic $r^{(a)}$ and neutral $r^{(n)}$ contributions, i.e.

$$r = r^{(a)} + r^{(n)} \tag{30}$$

$$r^{(a)} = a_{H^+}^n \, \Omega (\rho_s(1 - \varphi)) \, k_{ref}^{(a)} \exp\left(-\frac{E^{(a)}}{R}\left(T^{-1} - T_{ref}^{-1}\right)\right)(1 - \overline{SR}^p)^q, \tag{31}$$

$$r^{(n)} = \Omega(\rho_s(1 - \varphi)) \, k_{ref}^{(n)} \exp\left(-\frac{E^{(n)}}{R}\left(T^{-1} - T_{ref}^{-1}\right)\right)(1 - \overline{SR}^p)^q, \tag{32}$$

where a_{H^+} is activity of H$^+$, Ω is a constant reactive surface area, ρ_s is rock matrix molar density, T_{ref} and k_{ref} are reference temperature and reaction constant evaluated at reference temperature respectively, E is activation energy, R is gas constant, and SR denotes the upper-bounded saturation ratio $SR = \min(SR, SR_{max})$. While saturation ratio represents the tendency of a mineral to dissolve (SR < 1) or precipitate (SR > 1), the multiplier $(1 - SR_p)_q$ (Lassin et al., 2018), introduced by the Transition Rate Theory (Aagaard and Helgeson,

1982; Lasaga, 1981), measures the proximity of the heterogeneous reaction system to equilibrium. The parameters defining reaction kinetics are also listed in Tab. 7.

Fig. 7 shows pressure, element compositions and porosity profiles evaluated for the 1D homogeneous domain at $t = 0.1$ d and $t = 1$ d. Propagation of carbon dioxide deeper into the domain dissolves the calcite matrix enhances permeability and decreases the pressure gradient within the dissolved region. Fig. 8 demonstrates simulation results obtained for 2D heterogeneous domain at $t = 9$ d and $t = 42$ d. Heterogeneity distorts uniform dissolution front resulting in wormhole propagation.
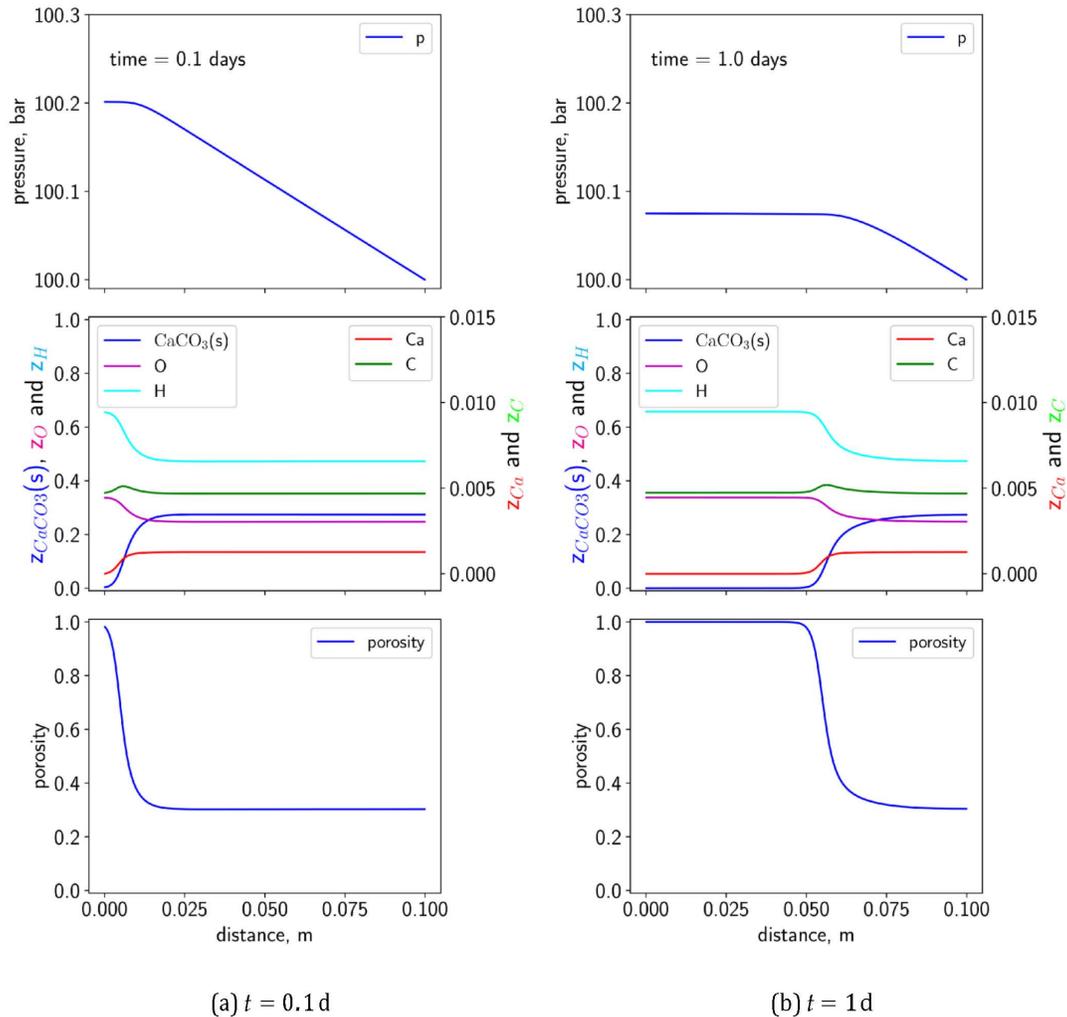

(a) $t = 0.1$ d   (b) $t = 1$ d

Figure 7—Profiles of pressure, element compositions and porosity obtained in the simulation of 1D configuration at $t = 0.1$ d (a) and $t = 1$ d (b).

Tab. 8 presents the performance metrics for simulation runs in 1D and 2D configurations, both with and without caching of OBL operators. The results clearly indicate that the major part of simulation time in both configurations is consumed by the sampling of OBL operators, i.e. by point generation. This accounts for over 90% of the total simulation time in the 1D case and more than 80% in the 2D case. The high computational cost of point generation is primarily attributed to the associated PHREEQC simulations, which calculate geochemical speciation, phase equilibrium and reaction kinetics. The table further highlights that caching OBL operators significantly reduces simulation costs by minimizing the need for repeated PHREEQC simulations in subsequent runs. It is important to note that the time metrics reported in Tab. 8, which are based each on single simulation run, may vary between runs and, therefore, are shown only for qualitative performance assessments. Additionally, these simulations incorporate the sequential

execution of PHREEQC while parallel extension can further alleviate costs of incorporated PHREEQC simulations.

Table 8—Performance metrics of modeling 1D and 2D configurations. MLin stands for multilinear interpolation while N denotes a number of supporting points uniformly distributed over each axes of the state space. The interpolation and point generation times are given in percent of the total simulation time. TS, NI and LI are the total numbers of time steps, nonlinear and linear iterations respectively. The timesteps and iterations wasted due to lack of convergence are listed in brackets.

Method	n_c	N	Cached	Time, sec	Interp., %	Point gen., %	TS	NI	LI
				1D setup, 500 cells					
MLin	5	501	✗	152.4	0.7	96.3	265	1060	3318
MLin	5	501	✓	4.8	28.4	1.5	265	1060	3318
				2D setup, 100 × 100 cells					
MLin	5	201	✗	1343.4	6.0	81.7	624	2726	41792
MLin	5	201	✓	819.0	15.2	6.6	625(1)	2729(20)	43657(144)
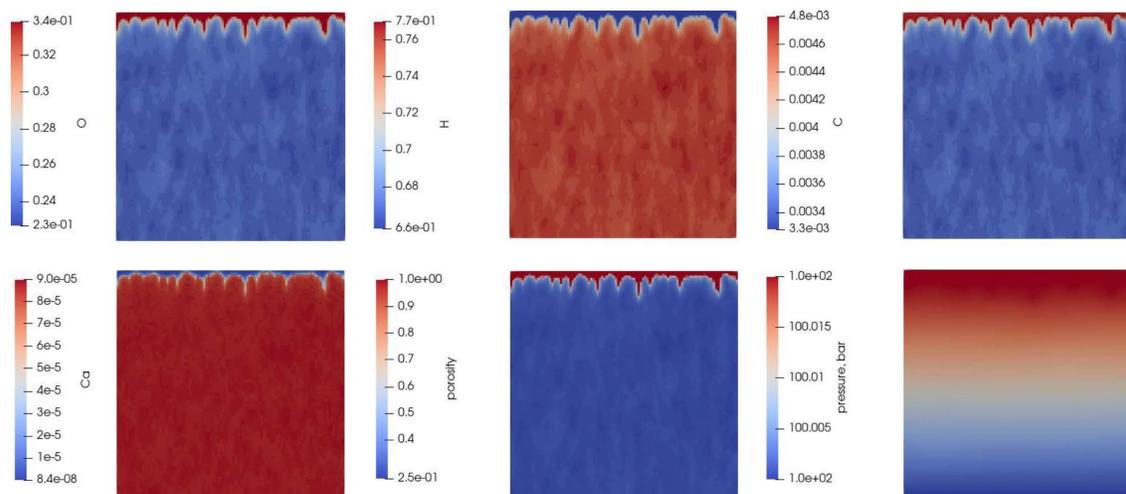
(a) $t = 9$ d.
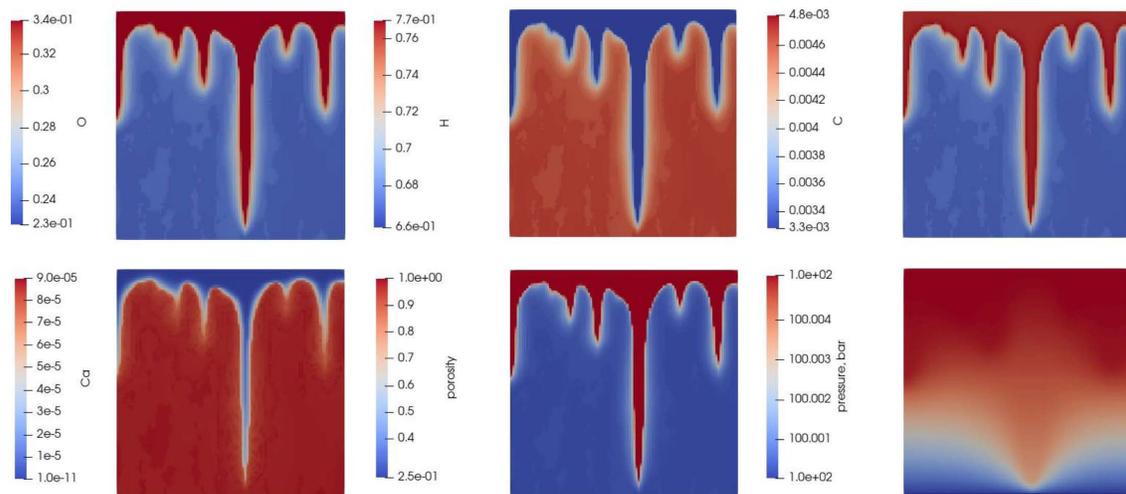
(b) $t = 42$ d.

Figure 8—Compositions of elements, porosity and pressure estimated at $t = 9$ d (a) and $t = 42$ d (b) after the start of injection into 2D configuration.

Conclusion

In this study, we investigated interpolation strategies required for evaluating state-dependent operators within the OBL approach. We compared multilinear and linear interpolation strategies, with the latter performed on both standard and Delaunay triangulations of a unit hypercube. A series of comparative studies was conducted using a two-phase multicomponent fluid model across multiple domain configurations, including homogeneous 1D and 2D domains as well as a heterogeneous 3D domain. The study revealed the following key findings:

- Simulations employing multilinear interpolation exhibited superior convergence compared to those using linear interpolation.
- For linear interpolation, standard triangulation demonstrated better performance than Delaunay triangula- tion due to the time-consuming simplex location process required for Delaunay triangulation.
- Multilinear interpolation remained efficient for state space dimensionalities $n_d \leq 8$ but incurred significant computational costs at higher dimensions.
- Linear interpolation emerged as the preferred and more robust approach for state space dimensionalities $n_d > 8$.
- The OBL approach was demonstrated to be applicable for state space dimensionalities up to $n_d = 20$.

Furthermore, we demonstrated the efficiency of the OBL approach when coupled with third-party solvers. We performed the simulation of CO_2 injection involving numerous chemical reactions, including dissolution- precipitation kinetics. PHREEQC simulator was employed to calculate geochemical speciation, phase equilib- rium, and reaction kinetics. The relatively high computational cost of PHREEQC simulations was significantly reduced through the caching of OBL operators.

In conclusion, caching sampled properties is critical for achieving high performance in multiphase- reactive- compositional modeling. This is particularly essential for highly nonlinear problems, especially when integrating third-party solvers. With sufficient property sampling, both multilinear and linear interpolation strategies can ensure efficient Jacobian assembly. The effectiveness of these techniques has been demonstrated within the OBL framework, which also provides the flexibility needed to reduce development costs in general-purpose modeling of geo-energy applications.

Acknowledgements

References

Aagaard, P. and Helgeson, H. (1982). Thermodynamic and kinetic constraints on reaction rates among minerals and aqueous solutions. i. theoretical considerations. *American Journal of Science*, **282**(3):237–285.

Acs, G., Doleschall, S., and Farkas, E. (1985). General purpose compositional model. *Society of Petroleum Engineers journal*, **25**(4):543–553.

Ahusborde, E., Amaziane, B., de Hoop, S., El Ossmani, M., Flauraud, E., Hamon, F. P., Kern, M., Socie, A., Su, D., Mayer, K., Toth, M., and Voskov, D. (2024). A benchmark study on reactive two-phase flow in porous media: Part ii - results and discussion. *Computational Geosciences*, **28**(3):395–412.

Coats, K. H. (1980). Equation of state compositional model. *Society of Petroleum Engineers journal*, (5):363–376.

Collins, D., Nghiem, L., Li, Y.-K., and Grabenstetter, J. (1992). Efficient approach to adaptive-implicit compositional simulation with an equation of state. *SPE Reservoir Engineering (Society of Petroleum Engineers)*, **7**(2):259–264.

de Hoop, S., Voskov, D., Ahusborde, E., Amaziane, B., and Kern, M. (2024). A benchmark study on reactive two-phase flow in porous media: Part i - model description. *Computational Geosciences*, **28**(1):175–189.

Fan, Y., Durlofsky, L. J., and Tchelepi, H. A. (2012). A fully-coupled flow-reactive-transport formulation based on element conservation, with application to co2 storage simulations. *Advances in Water Resources*, **42**:47–61.

Farshidi, S. F., Fan, Y., Durlofsky, L. J., and Tchelepi, H. A. (2013). Chemical reaction modeling in a compositional reservoir-simulation framework. volume **2**, page 1417–1438.

Fenghour, A., Wakeham, W., and Vesovic, V. (1998). The viscosity of carbon dioxide. *Journal of Physical and Chemical Reference Data*, **27**(1):31–39.

K. Aziz, (1979). Petroleum Reservoir Simulation. Applied Science Publishers LTD.

Kala, K. and Voskov, D. (2020). Element balance formulation in reactive compositional flow and transport with parameteri- zation technique. *Computational Geosciences*, **24**(2):609–624.

Khait, M. and Voskov, D. (2018). Operator-based linearization for efficient modeling of geothermal processes. *Geothermics*, **74**:7–18.

Khait, M. and Voskov, D. (2021). A gpu-based integrated simulation framework for modelling of complex subsurface applications. volume Day 1 Tue, October 26, 2021, page D011S010R004.

Lasaga, A. C. (1981). CHAPTER 4. TRANSITION STATE THEORY, pages 135–170. De Gruyter, Berlin, Boston.

Lassin, A., Andre, L., Devau, N., Lach, A., Beuvier, T., Gibaud, A., Gaboreau, S., and Azaroual, M. (2018). Dynamics of calcium carbonate formation: Geochemical modeling of a two-step mechanism. *Geochimica et Cosmochimica Acta*, **240**:236–254.

Lyu, X., Khait, M., and Voskov, D. (2021). Operator-based linearization approach for modeling of multiphase flow with buoyancy and capillarity. *SPE Journal*, **26**(04):1858–1875.

Lyu, X. and Voskov, D. (2023). Advanced modeling of enhanced co2 dissolution trapping in saline aquifers. *International Journal of Greenhouse Gas Control*, **127**:103–907.

McGeady, C. (2024). Powering the commanding heights: The strategic context of emergent u.s. electricity demand growth. *CSIS Briefs*. Energy Security and Climate Change Program.

Michelsen, M. L. (1982). The isothermal flash problem. part ii. phase-split calculation. *Fluid Phase Equilibria*, **9**(1):21–40.

Moyner, O. (2024). Jutuldarcy.jl - a fully differentiable high-performance reservoir simulator based on automatic differenti- ation. **2024**(1):1–37.

Parkhurst, D. L. and Appelo, C. A. J. (2013). Description of Input and Examples for PHREEQC Version 3—A Computer Program for Speciation, Batch-Reaction, One-Dimensional Transport, and Inverse Geochemical Calculations, volume **6** of *Techniques and Methods*. *U.S. Geological Survey*. Available only at http://pubs.usgs.gov/tm/06/a43/.

R. Byron Bird, Warren, E. Stewart, E.N.L. (2002). Transport phenomena. J. Wiley, 2nd, wiley international ed edition.

Voskov, D., Saifullin, I., Novikov, A., Wapperom, M., Orozco, L., Seabra, G. S., Chen, Y., Khait, M., Lyu, X., Tian, X., de Hoop, S., and Palha, A. (2024). Open delft advanced research terra simulator (open-darts). *Journal of Open Source Software*, **9**(99):6737.

Voskov, D. V. (2017). Operator-based linearization approach for modeling of multiphase multi-component flow in porous media. *Journal of Computational Physics*, **337**:275–288.

Voskov, D. V. and Tchelepi, H. A. (2012). Comparison of nonlinear formulations for two-phase multi-component eos based simulation. *Journal of Petroleum Science and Engineering*, **82-83**:101–111.

Wapperom, M., Lyu, X., Nichita, D. V., and Voskov, D. (2023). A unified thermal-reactive compositional simulation frame- work for modeling co2 sequestration at various scales. Day 2 Wed, March 29, 2023.

Weiser, A. and Zarantonello, S. E. (1988). A note on piecewise linear and multilinear table interpolation in many dimensions. *Mathematics of Computation*, **50**(181):189–196.

Young, L. C. (2022). Compositional reservoir simulation: A review. *SPE Journal*, **27**(05):2746–2792.

Younis, R. and Aziz, K. (2007). Parallel automatically differentiate data-types for next generation simulator development. page 487–502.

Zaydullin, R., Voskov, D., and Tchelepi, H. (2013). Nonlinear formulation based on an equation-of-state free method for compositional flow simulation. *SPE Journal*, **18**(2):264–273.

Zhou, Y., Tchelepi, H., and Mallison, B. (2011). Automatic differentiation framework for compositional simulation on unstructured grids with multi-point discretization schemes. volume **1**, page 607–624.